ASME Paper Title: Influence of Vortex Induced Loads on the Motion of SPAR-Type Wind Turbine: A Coupled Aero-H Vortex-Mooring Investigation

Authors: Yan Li, Liqin Liu, Qiang Zhu, Ying Guo, Zhiqiang Hu and Yougang Tang

ASME Journal Title: Journal of Offshore Mechanics and Arctic Engineering

Volume/Issue 140(5)

Date of Publication (VOR* Online) 21/05/2018

ASME Digital Collection URL: http://offshoremechanics.asmedigitalcollection.asme.org/article.aspx?articleid=26796

DOI: https://doi.org/10.1115/1.4040048

Influence of Vortex Induced Loads on the Motion of SPAR-Type Wind Turbine: A Coupled Aero-Hydro-Vortex-Mooring Investigation

Yan Li
State Key Laboratory of Hydraulic Engineering Simulation and Safety, Tianjin University
Tianjin, 300072, China
Department of Structural Engineering, University of California San Diego
La Jolla, CA 92093, USA
Collaborative Innovation Center for Advanced Ship and Deep-Sea Exploration
Shanghai, 200240, China
E-mail: liyan_0323@tju.edu.cn

Liqin Liu
State Key Laboratory of Hydraulic Engineering Simulation and Safety, Tianjin University
Tianjin 300072, China
E-mail: liuliqin@tju.edu.cn

Qiang Zhu
Department of Structural Engineering, University of California San Diego
La Jolla, CA 92093, USA
E-mail: qizhu@ucsd.edu

Ying Guo
State Key Laboratory of Hydraulic Engineering Simulation and Safety, Tianjin University
Tianjin 300072, China
E-mail: yynocry@tju.edu.cn

Zhiqiang Hu
School of Engineering, Newcastle University
Newcastle upon Tyne, NE1 7RU, United Kingdom
E-mail: zhiqiang.hu@ncl.ac.uk

Yougang Tang[1]
State Key Laboratory of Hydraulic Engineering Simulation and Safety, Tianjin University
Tianjin 300072, China
E-mail: tangyougang_td@163.com

[1] Corresponding author: Yougang Tang; E-mail: tangyougang_td@163.com

Abstract

The nonlinear coupling effect between DOFs and the influence of vortex induced loads on the motion of SPAR type FOWT are studied based on an aero-hydro-vortex-mooring coupled model. Both first- and second-order wave loads are calculated based on the 3D potential theory. The aerodynamic loads on the rotor are acquired with the blade element momentum theory. The vortex induced loads are simulated with CFD approach. The mooring forces are solved by the catenary theory and the nonlinear stiffness provided by the SPAR buoy are also considered. The coupled model is set up and a numerical code is developed for calculating the dynamic response of a Hywind SPAR-type FOWT under the combined sea states of wind, wave and current. It shows that the amplitudes of sway and roll are dominated by lift loads induced by vortex shedding, and the oscillations in roll reach the same level of pitch in some scenarios. The mean value of surge is changed under the drag loads, but the mean position in pitch, as well as the oscillations in surge and pitch, is little affected by the current. Due to the coupling effects, the heave motion is also influenced by vortex-induced forces. When vortex-shedding frequency is close to the natural frequency in roll, the motions are increased. Due to nonlinear stiffness, super-harmonic response occurs in heave, which may lead to internal resonance.

Keywords: *floating offshore wind turbines, coupled model, current, vortex induced motion, internal resonance, nonlinear stiffness, super-harmonic*

1. Introduction

With growing demands, the problem of energy shortage attracts more and more attention all over the world. Among different technologies, wind turbines convert wind energy into electricity with no pollution or waste [1]. Because of the greater intensity and stability of the offshore wind, the capacity of offshore wind turbine usually surpasses that of the onshore ones [2,3]. With the development of offshore technology, the research on offshore wind turbines is moving towards the deep-water zone. Compared with the fixed offshore wind turbine, the advantage of the floating offshore wind turbine (FOWT) is pronounced in the aspects of economy, convenience of installation and total capacity [4].

At present, the design of FOWT is based on experiences from offshore oil and gas production platforms [5]. Based on the floating foundations, FOWTs can be divided into barge, SPAR, semi-submersible and tension-leg-platform (TLP) types. During the past decades, full-scale prototypes of FOWT have been successfully launched and tested all over the world, greatly expediting the development of FOWT technologies [6]. Among those designs, the SPAR-based wind turbine tethered by multiple cables shows robust hydrodynamic performance [7].

With incoming currents, vortex induced vibration (VIV) is an important source of disturbance on offshore structures such as risers, pipelines [8-12], and FOWTs. When the vortex induced loads act on a rigid body with long and round shape but also large displacement, it will hardly cause any structural vibration but may induce additional motion in some degree of freedom (DOF) under specific conditions. This phenomenon is called Vortex Induced Motions (VIM). Maija and Benitz[13] studied the dynamic response of DeepCWind semi-submersible FOWT with incoming currents based on OpenFOAM. They found that the vortex shedding would cause large time-varying load, which affects the fatigue life of the system. Kokubun et.al. [14] conducted a 1/34.5 scaled model test, and recorded VIM frequency in sway, roll and mooring tension. Duan et. al. [15] performed model testing with various current, wind and wave conditions. The lock-in phenomenon of sway in the cross-flow direction was observed and the remaining responses, including the other 4-DOF motions, mooring tensions, and turbine bearing loads, were found to be coupled *via* sway/surge VIMs.

In previous studies, CFD approaches have been widely adopted in VIV investigations with slender risers. Li et.al [39] employed a partitioned iterative scheme based on Petrov–Galerkin formulation to simulate the VIV of an elastically mounted circular cylinder with 2D and 3D models, in which the wall proximity effects were observed. Mitta [40] examined the VIV of a circular cylinder with a stabilized space–time finite element formulation and identified three branches in the response. Bourguet et. al [41] investigated the multi-frequency VIV of a cylindrical tensioned beam under the scenario of shear flows. They found that the structural responses were determined by the shape of inflow profile. Wang et.al proposed a 3D fluid-structure interaction model to simulate the 2DOF VIV characters of a vertical riser [42,43], and observed different vortex shedding modes. Furthermore, a model was developed to simulate the couple VIV effect of two tandem flexible cylinders [44].

The hydrodynamic significance of VIM was widely studied in slender structures including the SPAR platform with both numerical methods and experimental approaches. Hirabayashi[16] numerically analyzed the VIM of 2D circular cylinders by using the lattice Boltzmann method, and the changing trends of lift load were observed in his work. Wu et.al [17] employed OpenFOAM to investigate the free vibration of a square cylinder in transient flow with three hybrid turbulence models. A 3D model was established in their simulation. The good agreement between their results and experimental data proves that the CFD approach is accurate enough to handle the vortex shedding problem for the VIM of a slender body.

Meanwhile, more work has been performed on the VIM of semi-submersible buoys, another group of slender structures. Hashiura et.al [18] conducted a series of towing experiments in water tank to investigate the relationship between the vortex induced force and the shape of buoy, as well as other parameters. Similarly, Liu et.al [19] carried out a group of model tests aiming at understanding the fluid physics associated with VIMs of deep-draft semi-submersibles. They found the wake behind the pontoons has non-negligible influence on the dynamic behavior of the buoy. Based on their experimental work, Liang et.al [20] further established 3D numerical models to simulate the vortex shedding in the wake as well as its effect on the motion of the rigid body.

Among the researches on SPAR platform, the wave-frequency motion and VIM are usually studied independently. In order to consider these effects simultaneously, Liu [21] created a coupled model for SPAR platform under the combined action of wave and vortex shedding caused by current. In his study, a 3-DOF model is developed to simulate the heave, roll and pitch of a SPAR. First-order wave force, second-order wave force and vortex induced force are considered in his numerical model, but the influence of mooring line is not included. Meanwhile, there are few researches on the SPAR-type floating wind turbine under the combined environmental loads of wave, wind and current.

In the present work, an in-house coupled model for SPAR-type FOWT is developed. Based on the potential flow theory, both first-order and second-order difference frequency wave forces are calculated with stochastic waves. The aerodynamic load on the wind turbine is calculated by the blade element momentum theory (BEM). The hydrodynamic coefficients of vortex are calculated by CFD approach. By coupling these modules in time domain, this method is capable of analyzing the dynamic response of SPAR-type FOWT under complex sea states.

In the following sections, the physical problem, including the configuration as well as physical parameters of the floating wind turbine system, is defined firstly. Afterwards, the numerical models (including the nonlinear restoring forces model, the catenary mooring model, the aerodynamics model, the vortex induced force model and the hydrodynamics model) are briefly described. Numerical results, including predictions of dynamic responses under wave, wind and current, are then presented. Finally, conclusions are drawn.

2. Physical problem

As shown in Fig. 1, the FOWT studied in this work consists of the NREL 5MW baseline wind turbine [22] (see Table 1) and a SPAR-type floating foundation with three mooing lines [23] (see Table 2). The mooring cables are located around the buoy body of the SPAR. One of the cables (Line #1) is directed along the positive x-axis in the xz-plane, and the other twolines (Line #2 and #3) are distributed uniformly around the platform. Hereby (x,y,z) is a Cartesian coordinate system with its origin at the mean free surface and z pointing upward. The x axis coincides with the direction of the incoming wind, wave and current.

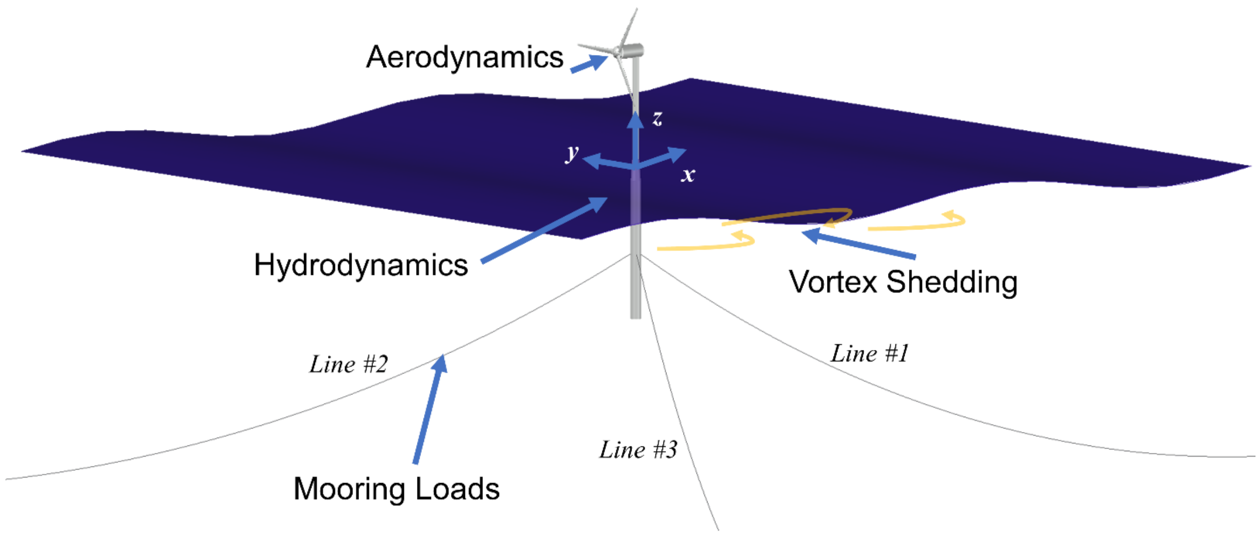

Fig.1 Definition of the physical problem

Table 1 Parameters of the NREL 5MW wind turbine

Parameter	Value
Rated power	5 MW
Shaft transmission efficiency	0.944
Radius of wind wheel	63 m
Radius of hub	1.5 m
Cut-in wind speed	3 m/s
Rated wind speed	11.4 m/s
Cut-out wind speed	25 m/s
Rated speed	12.1 rpm
Hub height(from the bottom of the tower)	90 m
CM location(from the bottom of the tower)	64.0 m
Total mass(including tower)	697,460 kg

Table 2 Parameters of the SPAR-type floating foundation and the mooring system

Parameter	Value
Depth to platform base below the SWL	120.0 m
Elevation to platform top above the SWL	10.0 m
Depth to top of taper below the SWL	4.0 m
Depth to bottom of taper below the SWL	12 m
Platform diameter above taper	6.5 m
Platform diameter below taper	9.4 m
Platform mass, including ballast	7,466,330 kg
CM location below the SWL along platform centerline	89.9155 m
Number of mooring lines	3
Angle between adjacent lines	120 deg
Depth to anchors below SWL (water depth)	320 m
Depth to fairleads below the SWL	70 m
Radius to anchors from the platform centerline	853.87 m
Radius to fairleads from the platform centerline	5.2 m
Unstretched mooring line length	902.2 m
Mooring line diameter	0.09 m

3. Methodology

3.1 Dynamic equation in time domain

The dynamic equation is developed to calculate the displacement, velocity and acceleration of FOWT in time domain. For moored floating offshore structures, the dynamic response is solved under the effects of wind, wave, current and cable forces. Considering the 6-DOF motions (see Fig.2), the governing equation can be written in the time domain as following,

$$\left[\boldsymbol{M}+\boldsymbol{A}(\omega)\right]\ddot{x}+\boldsymbol{C}(\omega)\dot{x}+\boldsymbol{D}\boldsymbol{f}(\dot{x})+\boldsymbol{K}(x)x=\boldsymbol{q}(t,x,\dot{x}), \tag{1}$$

where $\boldsymbol{M}$ is the body mass and inertia matrix, $\boldsymbol{A}$ is the frequency-dependent added mass matrix, and $\boldsymbol{C}$ is the frequency-dependent radiation damping matrix. $\boldsymbol{D}$ is the nonlinear damping matrix. $\boldsymbol{f}$ is the vector function of $\dot{\boldsymbol{x}}$. $\boldsymbol{K}$ is the restoring matrix provided by buoyancy. $\boldsymbol{x}, \dot{\boldsymbol{x}}, \ddot{x}$ represent the 6-DOF position, velocity and acceleration vectors of the body, respectively. $\boldsymbol{q}$ is the exciting force vector, which includes the first- and second-order wave loads, the nonlinear restoring forces provided by the mooring lines, the vortex induced loads, and the aerodynamic loads on the rotor.

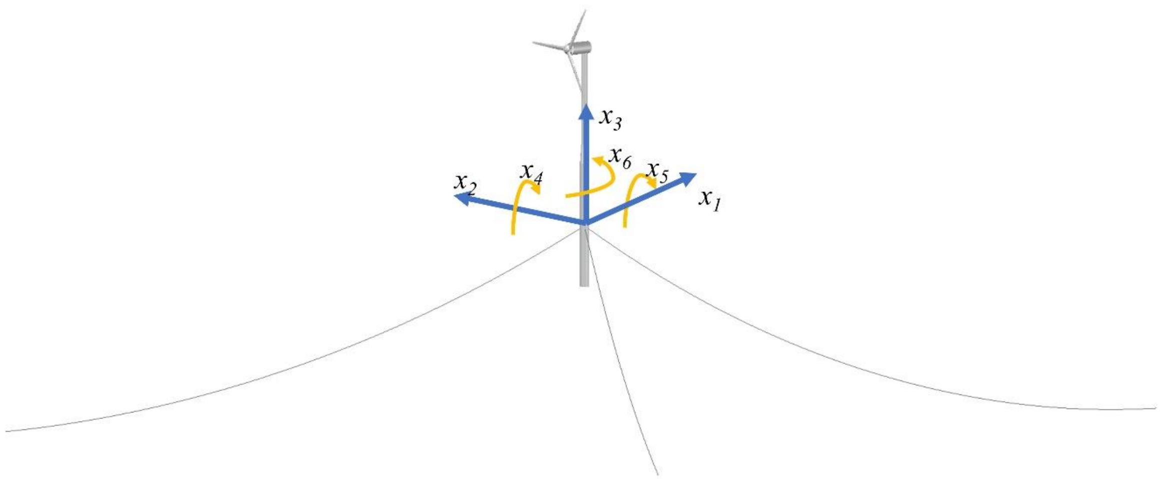

Fig.2 Six DOFs of FOWT

The added mass and radiation damping coefficients calculated based on the 3D potential theory are frequency dependent. With irregular waves, it is difficult to choose the corresponding added mass and damping coefficients for the time domain equations. In order to solve this problem, the frequency-dependent added mass and radiation damping coefficient are transferred into the added mass corresponding to the infinite frequency and retardation function based on the convolutional method [24]. Thus, the governing equation can be written as,

$$(\boldsymbol{M}+\boldsymbol{A}_\infty)\ddot{\boldsymbol{x}}(t)+\int_0^t \boldsymbol{h}(t-\tau)\dot{\boldsymbol{x}}(\tau)d\tau+\boldsymbol{Df}(\dot{\boldsymbol{x}})+\boldsymbol{K}(\boldsymbol{x})\boldsymbol{x}=\boldsymbol{q}(t,\boldsymbol{x},\dot{\boldsymbol{x}}), \tag{2}$$

where $\boldsymbol{h}(t)$ is the retardation function, and $\boldsymbol{A}_\infty$ is the added mass when the frequency approaches infinite.

3.2 Wave loads

The wave is assumed to propagate along the positive x-axis, and stochastic wave elevation $\eta(t)$ can be decomposed into the sum of N regular wave components as following,

$$\eta(t)=\sum_{n=1}^{N} a_n \cos(k_n x-\omega_n t+\varphi_n). \tag{3}$$

For each component, a_n denotes the wave amplitude, ω_n is the circular frequency, k_n is the wave number, and φ_n is the random phase angle. The wave amplitude a_n can be calculated by the corresponding wave spectrum S_η.

To obtain the wave force on the platform in time domain, the load transfer functions are calculated based on the 3D potential theory in frequency domain by using the DNVGL software WADAM. Specifically, the hydrodynamic transfer function includes linear transfer function (LTF) $F_1(\omega)$, as well as the sum-frequency quadric transfer function (QTF) $F_{2s}(\omega_i,\omega_j)$ and difference-frequency QTF $F_{2d}(\omega_i,\omega_j)$. Based on our previous analysis on SPAR-type FOWT [25], the second-order sum-frequency wave load will not significantly affect the dynamic response of the floating buoy due to its low natural frequencies. It is thus not included in the following simulations.

Afterwards, the random wave forces are transferred into time series by multiplying these hydrodynamic parameters and specified wave spectrum in the complex domain [26]. The real part of the complex expression will be the corresponding terms of wave loads in time domain so that we have,

$$F_{wave\_1}(t) = \mathrm{Re}\left[\sum_{i=1}^{M}\eta_i F_1(\omega_i)\right] = \mathrm{Re}\left[\sum_{i=1}^{M} a_i \exp\left[i\left(\omega_i t + \phi_i\right)\right] F_1(\omega_i)\right], \tag{4}$$

$$F_{wave\_2d}(t) = \mathrm{Re}\left[\sum_{i=1}^{M}\sum_{j=1}^{M}\eta_i \eta_j^* F_{2d}(\omega_i,\omega_j)\right] = \mathrm{Re}\left[\sum_{i=1}^{M}\sum_{j=1}^{M} a_i a_j \exp\left[i\left(\left(\omega_i-\omega_j\right)t+\phi_i-\phi_j\right)\right] F_{2d}(\omega_i,\omega_j)\right], \tag{5}$$

where η_i and η^*_i donate the elevation and its conjugation of *i*-th wave component in complex domain. a_i, ω_i and φ_i donate the amplitude, frequency and phase of *i*-th wave component as mentioned above, respectively.

3.3 Vortex induced loads

A two-dimensional cylinder model was developed to investigate the vortex shedding and its induced loads on the SPAR buoy. The CFD package Fluent is adopted to calculate the lift and drag coefficients, as well as the vortex shedding frequency. Based on these results, the time varying distributed vortex induced lift and drag forces can be obtained as below,

$$F_L(t) = \frac{1}{2} C_L \rho_c U_\infty^2 D \cos(2\pi f_s t + \alpha), \tag{6}$$

$$F_D(t) = \frac{1}{2} C_{Dm} \rho_c U_\infty^2 D + \frac{1}{2} C_{Da} \rho_c U_\infty^2 D \cos(4\pi f_s t + \alpha), \tag{7}$$

where C_L and C_{Da} are the amplitudes of the lift and drag coefficients, respectively. C_{Dm} is the mean value of drag coefficients. ρ_c is the density of the current. U_∞ is the inflow velocity. D is the diameter of the SPAR buoy. f_s is the vortex shedding frequency, and α is the phase angle. Specifically, the oscillation frequency of the lift force is the same as the vortex shedding frequency, while that of the drag force is twice the vortex shedding frequency. [37]

The vortex induced loads act on the wet surface of the SPAR. Thus, the forces and moments can be calculated by integrating the distributed lift and drag forces along the depth *z*. We have

$$F_{v1}(t) = \int_{-h}^{0} F_D(t)dz \ , \tag{8}$$

$$F_{v2}(t) = \int_{-h}^{0} F_L(t)dz \ , \tag{9}$$

$$T_{v4}(t) = \int_{-h}^{0} F_L(t)(z - z_G)dz \ , \tag{10}$$

$$T_{v5}(t) = \int_{-h}^{0} F_D(t)(z - z_G)dz \ , \tag{11}$$

where z_g is the center of gravity. $F_{v1}(t)$ and $F_{v2}(t)$ represent the vortex-induced forces in surge and sway respectively, while $T_4(t)$ and $T_5(t)$ represent the vortex induced moments in roll and pitch.

3.4 Aerodynamic loads

Although it is a quasi-static algorithm, the Bladed Element Momentum (BEM) method has proven to be a simple but accurate way to calculate aerodynamic forces acting on the wind turbine blades, [27,28]. In this work, the BEM approach is adopted to simulate the aerodynamic loads applied on the rotor when the turbine operates.

Each blade is discretized into seventeen parts along the span. Within each part the blade elements have the same airfoil shape. The axial induction factor *a* and tangential induction factor *a'* can be calculated by iterations at each blade element based on the parameters of the airfoil, such as chord, local pitch angle etc. Then, thrust and torque at each element are determined. After the local aerodynamic loads for all control volumes are obtained, we can get the normal and tangential load distributions. The general thrust and torque on rotor can be acquired by integrating along the span. With these distributions, the aerodynamic performance of the rotor, such as thrust on rotor, power output and bending moment at the root of blade, could be analyzed. A tip loss model, hub loss model and Glauert correction are also adopted to fix the induction factor due to finite blade number vortex shedding from the hub, and turbulent wake. Besides, the motion-induced and vortex-induced velocities of the floating foundation are also considered. Further details on the BEM approach could be found in [29].

In this study, the airfoil data of the NREL-5MW wind turbine are adopted [22]. Both the lift and drag coefficients are corrected for rotational stall delay and the drag coefficients are also corrected using the Viterna method. The detailed correction progress could be found in [22]. To validate our aerodynamic model, the thrust on the rotor as well as the output power is calculated. These results are then compared with the data in [22] (Fig.3). It is shown that the accuracy of our model meets the requirement of the simulation.

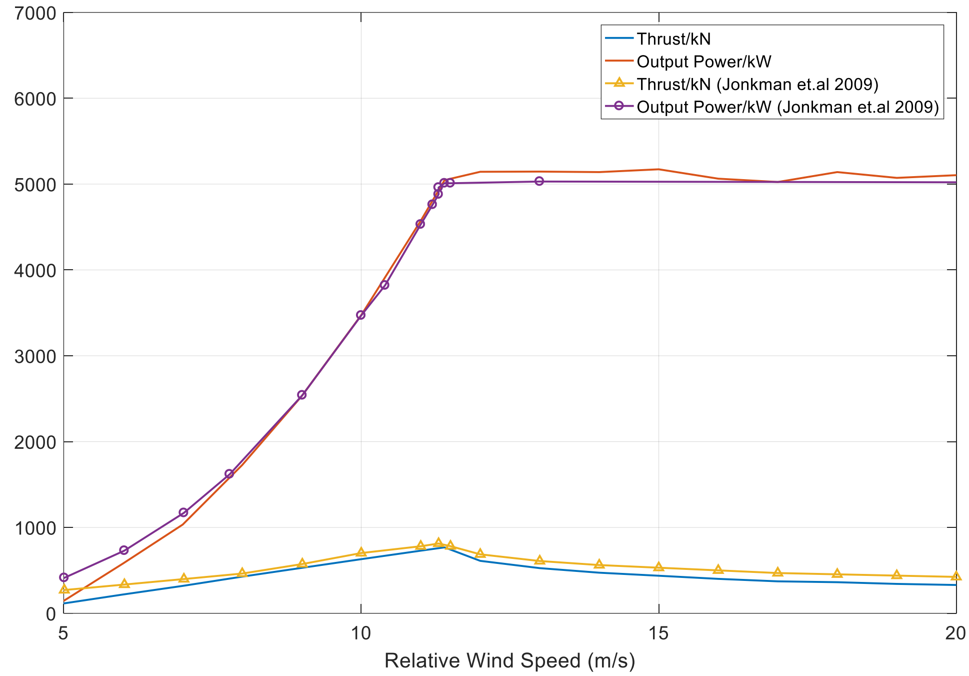

Fig.3 Validation of the aerodynamic model

3.5 Restoring forces

The nonlinear restoring forces of SPAR-type FOWT is composed of two parts. One part is provided by the mooring system, and the other is the hydrostatic force of the SPAR buoy. A separate module was programmed to calculate the tensions in each cable according to the catenary theory, a quasi-static algorithm to predict mechanics of the mooring system [30]. On the other hand, previous studies on SPAR show that the nonlinear restoring forces of this type floating foundation are mainly reflected in heave, roll and pitch [31,32]. Based on the geometric characteristics of SPAR platform, the additional restoring forces/moments in heave, roll and pitch can be expressed as

$$F_3 = \rho g A_w \left(-\eta - \frac{1}{2} H_g x_4^2 - \frac{1}{2} H_g x_5^2 \right), \tag{12}$$

$$M_4 = -\frac{1}{2} \rho g \left(\nabla + 2A_w \times \overline{GM_4} \right) x_3 x_4 + \frac{1}{2} \rho g \left(\nabla + 2A_w \times \overline{GM_4} \right) \eta x_4, \tag{13}$$

$$M_5 = -\frac{1}{2} \rho g \left(\nabla + 2A_w \times \overline{GM_5} \right) x_3 x_5 + \frac{1}{2} \rho g \left(\nabla + 2A_w \times \overline{GM_5} \right) \eta x_5, \tag{14}$$

where ρ denotes the density of water, g denotes the gravitational acceleration, A_w is the area of water line, ∇ is the displacement volume, $\overline{GM}_4$ and $\overline{GM}_5$ are the initial metacentric heights in roll and pitch, respectively, η denotes the elevation of wave, H_g denotes the height of center of gravity, x_3, x_4, and x_5 denote the heave, roll and pitch of the

SPAR buoy as shown in Fig.2. More details of derivation could be found in Refs. [31,32]. In our simulation, the nonlinear restoring load is a part of the external loads $\boldsymbol{q}$ in Eq. (2).

3.6 Flow chart of simulation

Based on the algorithms above, a coupled aero-hydro-vortex dynamic simulation tool for SPAR-type FOWT is developed in the time domain. The basic procedure of this coupled numerical simulation is shown in Fig. 4.

Before the time domain simulation begins, the initial conditions, hydrostatic and hydrodynamic coefficients are pre-generated. At each time step, the motions of COG are numerically calculated from Eq. (2) using the 4th order Runge-Kutta method. For simplicity, structural flexibility is not included in this model so that the wind turbine and floating platform are modeled as a rigid body. The motion of fairlead and rotor could also be calculated. Thus, the right-hand side of Eq. (2) could be updated for each module and integrated to the next time step.

Compared with the other existed codes, our simulation tool is specifically developed for the purpose of investigating the motion of SPAR-buoy FOWT under the complex sea states, specifically the VIMs caused by currents. Moreover, we take the nonlinear coupling effect between DOFs of SPAR buoy into consideration, which is usually not considered in other studies.

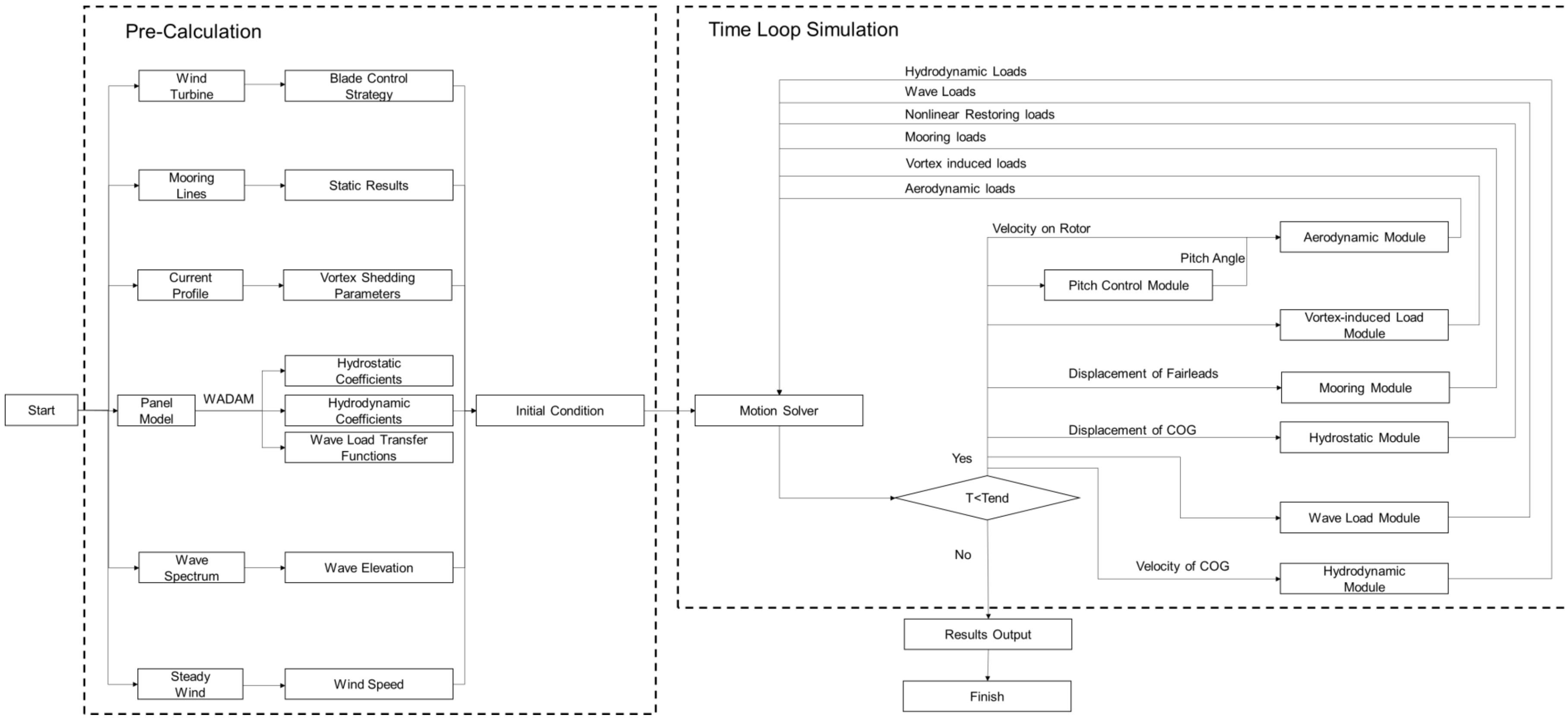

Fig.4 Basic procedure

4. Results

The coupled model is adopted to analyze the dynamic response of the SPAR-type FOWT under combined loads from wave, wind and current. Firstly, the vortex shedding phenomenon is simulated based on 2D CFD model, and the coefficients of vortex induced loads are presented. Then, free-decay tests are conducted to show the natural characteristics of FOWT. Afterwards, four different scenarios under the rated sea state are considered, referred to as cases 1 to 4 (see, Table 3). The details of environmental parameters can be found in Table 4. In the results, the focus is on motions of the platform, including the transverse, longitudinal and vertical motions. Furthermore, some nonlinear internal resonance phenomena are observed and discussed.

Tab.3 Definition of load cases

Load Case	Current	Wind	Wave
1	Uniform	-	-
2	-	Steady	Irregular
3	Uniform	Steady	Irregular
4	Shear	Steady	Irregular

Tab. 4 Environmental parameters

Parameter	Value
Wind speed	11.4 m/s
Surface velocity	0.6 m/s
Wave spectrum	JONSWAP
Significant wave height	6 m
Spectrum Peak Period	10s
Spectrum Peak Factor	3.3
Direction of wind, wave and current	Aligned,0°

Once the relative wind speed at the rotor exceeds the rated speed due to the induced velocity, the output power and aerodynamic force will increase rapidly. In order to keep the output power stable (and also for structural safety), a blade-pitch control system is necessary. In this study, a simplified quasi-static model is adopted [30]. The pitch angle is obtained *via* interpolation using the instantaneous wind speed with respect to the rotor, whose speed remains constant.

4.1 Vortex shedding induced loads

The configuration of our computational domain is sketched in Fig.5. According to previous research about the SPAR platform [21,38], the computational domain is a rectangular box with -5D < x < 20D and -5D < y < 5D, where D is the diameter of the SPAR centered at (0,0). The left side of the flow area is the inflow boundary and the right side is the outflow one. Considering the infinity of the flow, the upper and lower sides of the area are the symmetric boundary, and the surface of SPAR is set as non-slip boundary. The quadrilateral mesh is applied in the flow area and mesh refinements are performed in the area near the SPAR and the wake area. In the present work, we use 18250 elements in the flow field. The RNG k-ε model is chosen as the turbulence model, and the standard wall functions are adopted for enhancement. Based on previous assessments on the vortex shedding effect of rigid cylinder between 2D and 3D CFD approaches, it shows that the amplitude results of 2D model are about 10% lower than the 3D model results, but the vortex shedding frequency of 2D model results shows a good quantitative agreement with the 3D one [50]. Thus, in present study, the 2D CFD approach was adopted to simulate the vortex shedding around the cylinder.

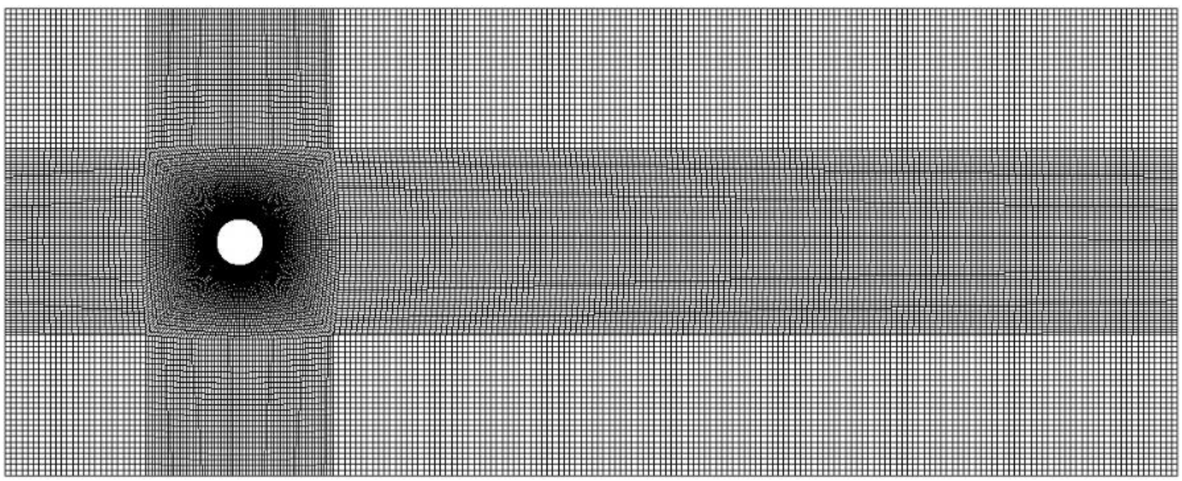

Fig.5 Mesh of the flow area

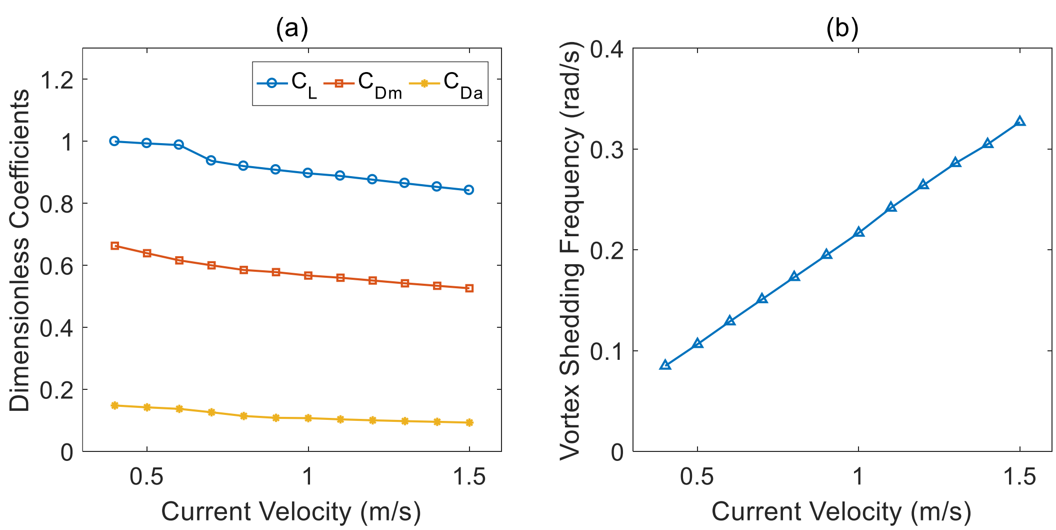

Fig.6 Hydrodynamic Coefficients and vortex-shedding frequency of SPAR buoy

The results under different current velocities are shown in Fig.6. From the results, it can be seen that both coefficients of lift and drag loads decrease with the increasing current velocity. On the other hand, by comparing the results of C_l and C_{Da}, it is found that the amplitude of lift is almost 10 times as that of drag, but the mean values of drag load are about 60% of the amplitude of lift. That is the reason why the drag loads are often neglected or treated as steady loads in most studies on VIV or VIM.

In the following simulations, both the harmonic lift and drag loads will be taken into account. According to the shape of wet surface, both SPAR buoy and flow are discretized along the depth. Specifically, the profile of the current in LC4 decreases linearly with the depth, and the velocity at the seabed is assumed to be 0. At different depths, the vortex induced loads are calculated by using different velocity and vortex induced hydrodynamic coefficients based on the CFD results in Fig.6.

4.2 Free-decay tests

In order to investigate the natural frequencies of the FOWT, a series of free-decay tests are conducted. In each simulation, an initial displacement was prescribed for the corresponding DOF (1m for translational motions and 0.1rad for rotational motions) before the FOWT was released. The time histories of the motions in 6 DOFs were then recorded. According to the Fast Fourier Transformation of the time histories, the natural frequencies are shown in Table 5.

Tab.5 Natural Frequencies of FOWT

DOF	Natural Frequency (rad/s)
Surge	0.050
Sway	0.050
Heave	0.207
Roll	0.163
Pitch	0.163

Another phenomenon observed during the free-decay tests is the coupling effect between heave, roll and pitch. Fig.7 presents the results with initial heel/trim angle. The time histories of heave and roll/pitch are shown in Fig.7(a) and (b), and the response spectra of heave and roll/pitch are presented in Fig.7(c). There are 2 peaks in response of roll/pitch and 3 peaks in heave (see Table 6). According to the natural frequencies of each DOF in Table.5, we find that the frequencies of roll mode correspond to the natural frequencies of sway and roll, respectively. That is to say, roll is coupled with sway. Similarly, pitch is coupled with surge.

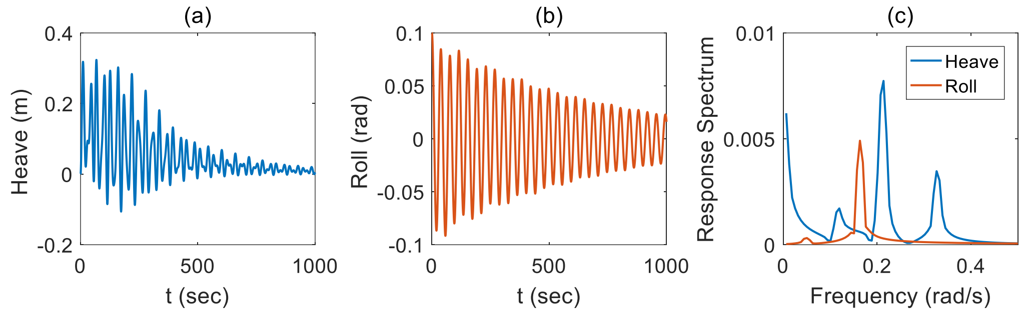

Fig.7 Coupling effects in free-decay tests of roll

Tab.6 Peak Frequencies of FOWT

DOF	Frequency (rad/s)		
	1st	2nd	3rd
Heave	0.113	0.207	0.326
Roll/Pitch	0.050	0.163	-

On the other hand, the response in heave is much more intriguing. Among the 3 peaks, the second one corresponding to the largest amplitude is the natural frequency of heave itself, and the other two correspond to super-harmonics of peak frequencies in roll. According to the nonlinear restoring force in Eq. (12), the heave mode is coupled with both roll and pitch. Based on the nonlinear dynamic theories, the second-order term of roll will induce these two-time-super-harmonic responses in heave, as the results show. The coupling effect between the DOFs will increase the response in some scenarios, and it will be further discussed later.

4.3 VIMs under the current loads (LC1)

To test the accuracy of our numerical model in simulating the VIM of SPAR-type FOWT, the responses under the current-only case (LC1) are calculated. The trajectories in the horizontal plane are shown in Fig.8 with different current velocities. It is seen that the VIMs display the figure-eight shape. These trajectories are qualitatively similar to the observed ones in model tests [15].

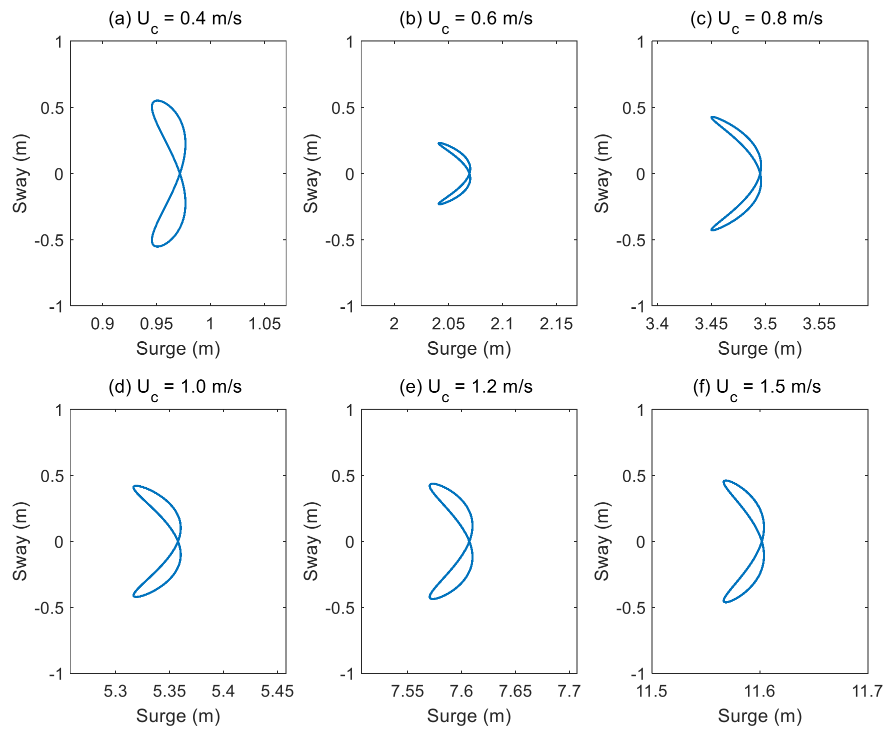

Fig.8 Trajectories of VIMs

Fig.8 indicates that the mean displacement in surge increases with the growing current velocity, but the amplitude of oscillation remains almost unchanged. The amplitude of sway is about 0.5m, much larger than that of surge. According to the results of model tests acquired with a 1/50 model [15], the oscillation in surge is in the range from 0.015m to 0.1m, and that of sway is from 0.015m to 0.15m. The oscillations in our numerical simulations are smaller than the results in the laboratory test. In fact, the model in our simulation is based on the full-scale model. While in the model tests, both the geometric parameters and current velocity are in small-scale, in order to meet the similarity of Froude number. Thus, the Reynolds number in the test is 1/354 of that of the full-scale prototype. Moreover, the configuration of mooring system and the water depth in the model test are also different from the model in our simulation. All these differences cause quantitative difference, whereas the trajectories of VIMs in the model test are quantitatively similar to results from our numerical simulations.

4.4 Motions under wind, wave and current

In this section, the effect of vortex induced force on the overall responses of the system is examined. The chosen load cases are LC2(No current), LC3(Uniform flow) and LC4(Shear flow). In LC4, the current profile is discrete into several parts along the depth, and the current velocity is assumed to be uniform in each part [45]. At different depths, the vortex induced loads are calculated by using the corresponding velocity and hydrodynamic coefficients. The coefficients of vortex induced load are shown in Table 7.

Tab. 7 Vortex induced hydrodynamic coefficients in LC3 and LC4

Current Velocity (m/s)	Upper Bound (m)	Lower Bound (m)	Diameter (m)	C_l	C_{dm}	C_{da}	ω_s (rad/s)
LC3 Uniform Flow							
0.600	0	-14	6.5	0.988	0.616	0.137	0.182
	-14	-128	9.4	0.983	0.623	0.141	0.129
LC4 Shear Flow							
0.587	0	-14.00	6.5	0.985	0.621	0.145	0.177
0.562	-14.00	-21.33	9.4	0.981	0.623	0.141	0.122
0.550	-21.33	-40.00	9.4	0.983	0.627	0.140	0.119
0.500	-40.00	-66.67	9.4	0.993	0.639	0.142	0.106
0.450	-66.67	-93.33	9.4	0.998	0.647	0.147	0.098
0.400	-93.33	-128.00	9.4	0.999	0.663	0.148	0.085

The proposed 2D approach to calculated the vortex shedding in both uniform and shear is based on previous researches [46-49], and the approaches are verified with 3D simulation in those work [46,47]. Specifically, in Ref. 46, a 1/100 scale model of cell-SPAR platform with a diameter of 0.368m is chosen to perform the validation with Fluent. Both model tests and numerical simulations (including 2D and 3D) are conducted with the case where the current velocity is 0.1 m/s, including uniform and shear profile. Because of the physical limitation, the case with shear current profile is only simulated numerically. According to the results, although the 2D results are slightly larger than the 3D ones, 2D simulation meets the requirements of accuracy and efficiency. It is true that 3D-based models are physically more accurate, especially in cases with shear current profile and turbulence effects. However, these models are still too expensive. On the other hand, the results of natural period, which is one of the key mechanism to the nonlinear analysis, are more accurate in 2D simulations. Hence, this approach was adopted in our simulation.

In the following simulations, the overall time is 3600 and the time step is 0.1 sec. After the first 500 sec, the initial start-up transient effect has faded and the FOWT is oscillating around its dynamic equilibrium position, so the rest samples (31000) are used for statistic and FFT analysis. The results are shown in Fig.9. Among these results, three different topics are majorly discussed in the following sections, which are transvers longitudinal and vertical motions, respectively.

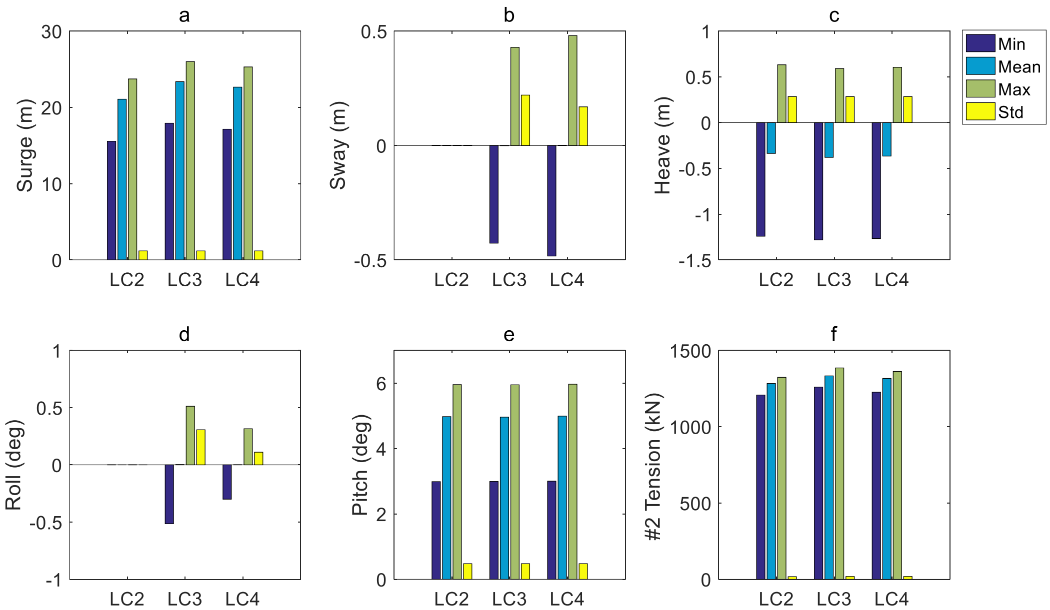

Fig.9 Statistic results of motions and mooring tensions

4.4.1 Transverse Loads and Motions

The results of sway and roll are shown in Fig.10 and Fig.11. To distinguish the curves clearly, the logarithmic scale is adopted for the response spectra in the following subsections. Since the value of transverse loads and motions in LC2 keeps zero, they are not shown in the logarithmic spectra. Based on the time histories of lift loads in Fig. 10a and Fig11a, multi-frequency vortex induced loads are applied on the transverse DOFs of FOWT when the current is present. Among the components in the spectra of lift loads (Fig. 10b and Fig. 11b), the responses whose frequencies correspond to the part of the buoy with a diameter of 9.4m are larger than others (Table. 7). It is attributed to the longer wet buoy of the 9.4-meter-diameter part.

According to the statistic results of sway in Fig.9b and roll in Fig.9d, as well as the time histories in Fig.10c and 11c, it can be seen that the amplitudes in sway and roll increase significantly with the vortex induced load taken into consideration, but the mean positions keep unchanged. The response spectra of these motions are presented in Fig. 10d, 11d. It shows that the frequencies of sway and roll are in agreement with the corresponding frequencies of lift loads. These are also the vortex shedding frequencies.

Moreover, the effect of flow profile can be seen by comparing the results of LC3 and LC4. On one hand, there exists significant difference in the lift force between LC3 (uniform current) and LC4(shear current). The difference in the lift moments on roll is smaller than that on sway. With these differences, both the roll and sway amplitudes in LC4 are smaller than those in LC3.

This is caused by the decreasing flow velocity with the increasing depth in LC4, which reduces the amplitudes of lift loads. On the other hand, the frequencies of vortex shedding in LC4 are more complicated because of the variation of velocity on different layers (Table. 7). This leads to the occurrence of more frequencies in the transverse motion.

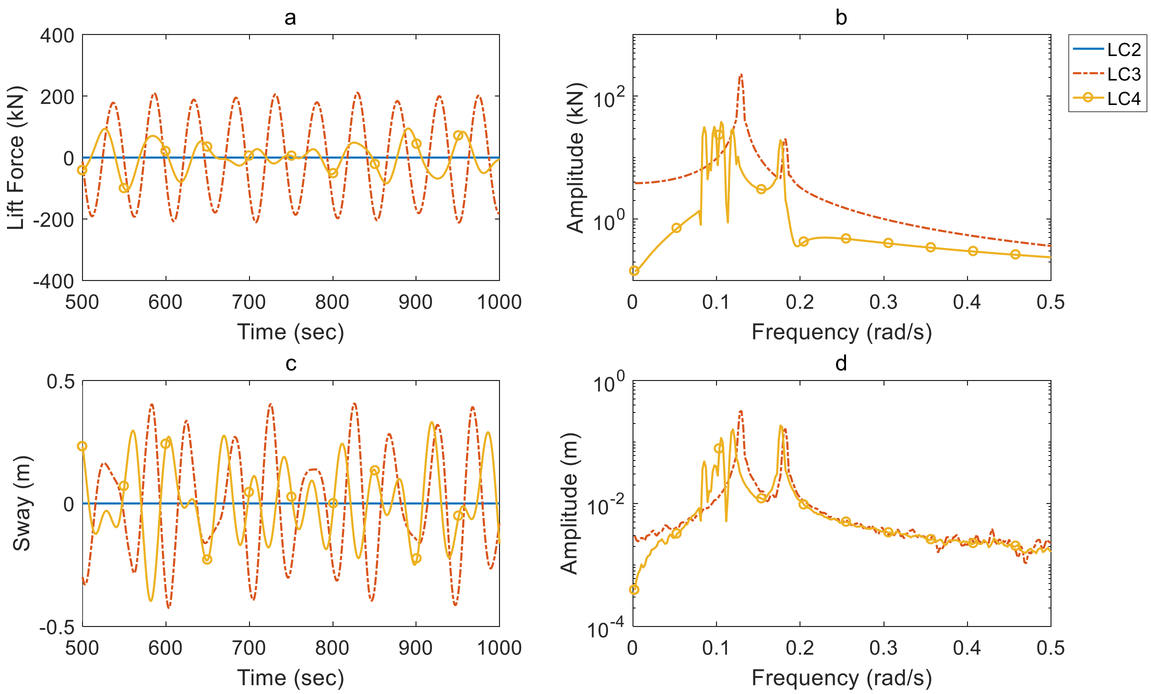

Fig.10 Time histories and response spectra of sway and lift force

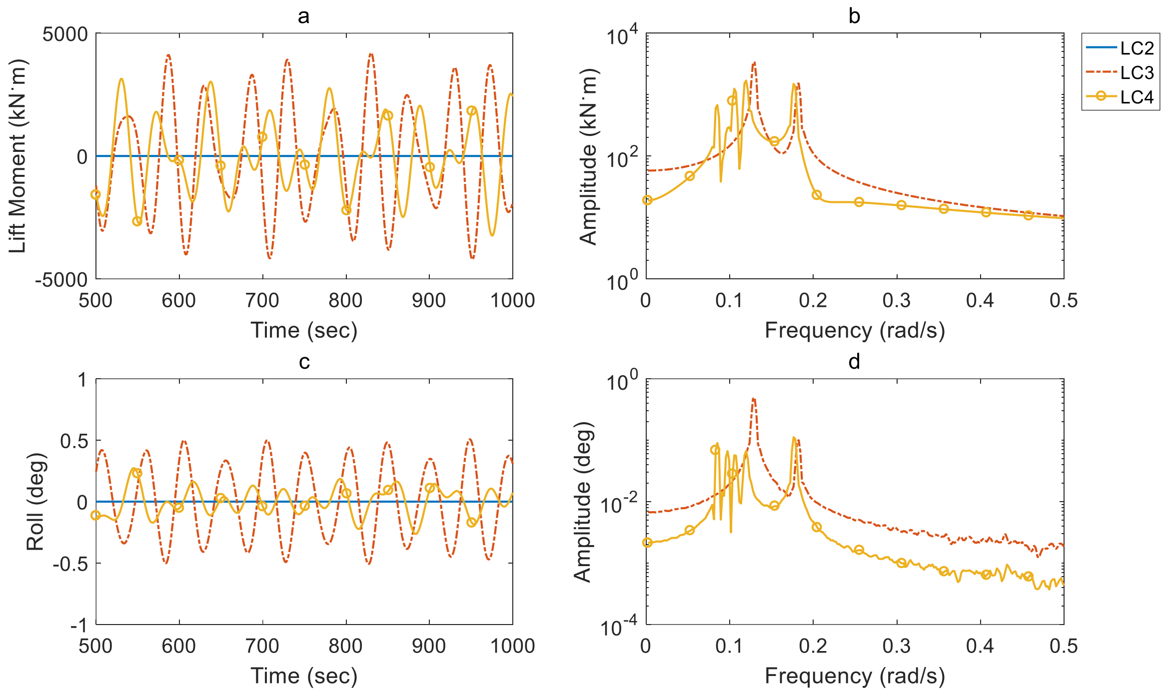

Fig.11 Time histories and response spectra of roll and lift moment

4.4.2 Longitudinal Motions

To examine the effect of the time-varying drag loads on the longitudinal motions, in Fig.12 we show the vortex shedding loads and dynamic response in surge, and those results in pitch are presented in Fig.13. It is seen from the time histories that the mean position in surge is enlarged when the drag force is applied, while the trim angle of FOWT keeps unchanged. On the other hand, both the time histories and spectra show that the oscillations in surge and pitch are almost the same in these three cases. It leads to the graphically indistinguishable curves in the response spectra of all cases, even though the logarithmic scale is used. To summarize, unlike the transverse motions, only the mean position in surge is significantly affected by the current, other features of longitudinal motions are little changed.

The explanation of these phenomena lies in the characteristics of the drag loads. From Fig.12a and 13a, it is seen that there exists significant difference in the mean values of drag force in different cases, and it causes the difference in the mean position under different currents. On the other hand, due to the similarity in the drag moments in pitch, the mean position in pitch is less affected. Moreover, according to the spectra, the frequencies of drag loads in LC4 is more spread than those in LC3. The oscillatory amplitude of drag is an order of magnitude less than the one of lift. As the frequencies of drag are two times those of lift, they are thus far away from the natural frequencies of surge and pitch, the oscillations in these modes are less affected.

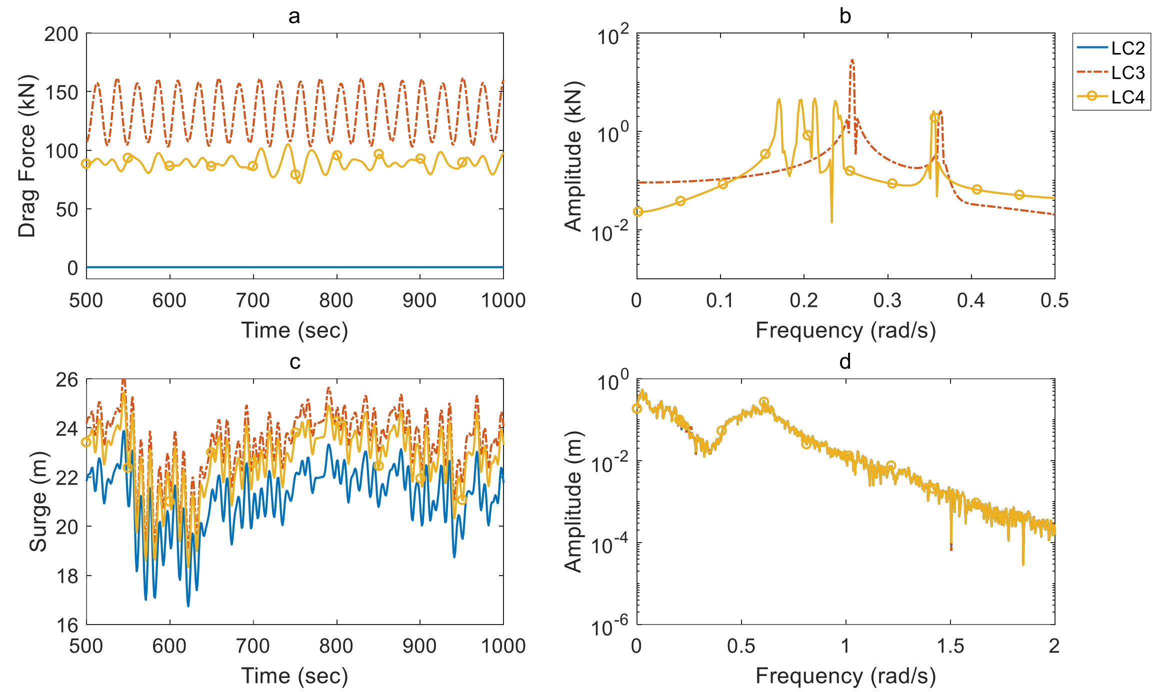

Fig.12 Time histories and response spectra of surge and drag force

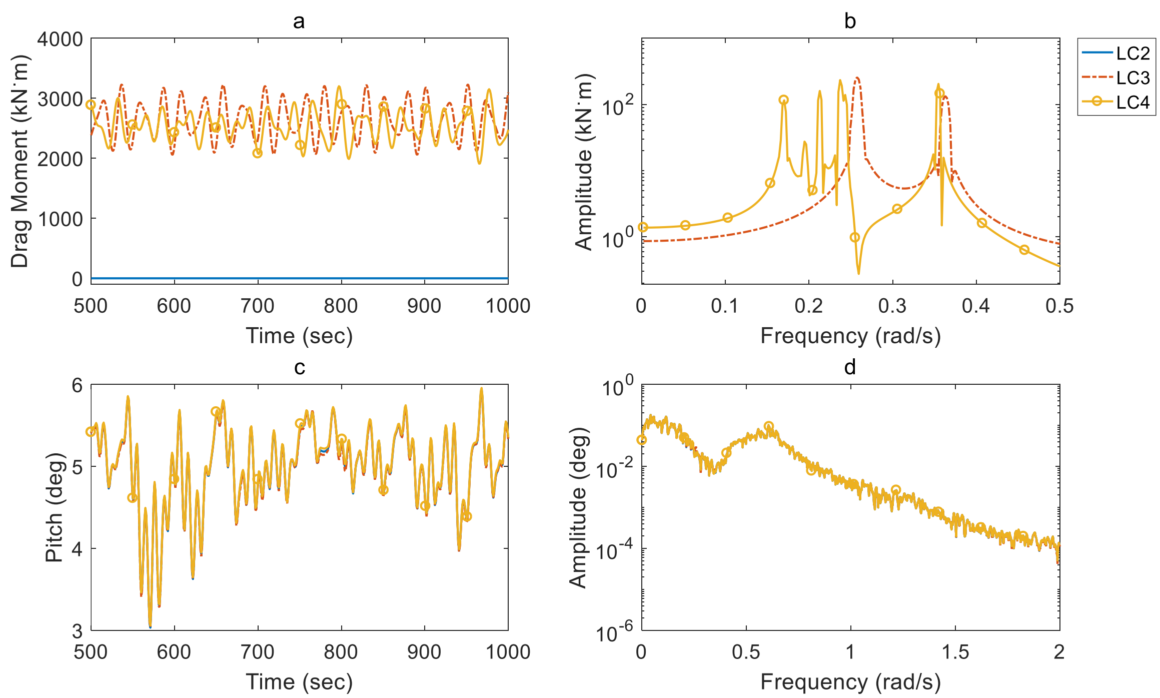

Fig.13 Time histories and response spectra of pitch and drag moment

On the other hand, the magnitude of drag and wave loads on the platform are displayed in Fig.

14. According to the time histories, we found that the mean level of wave loads in surge and pitch are much larger than the vortex induced loads. In other words, the longitudinal oscillations are mostly determined by the wave forces.

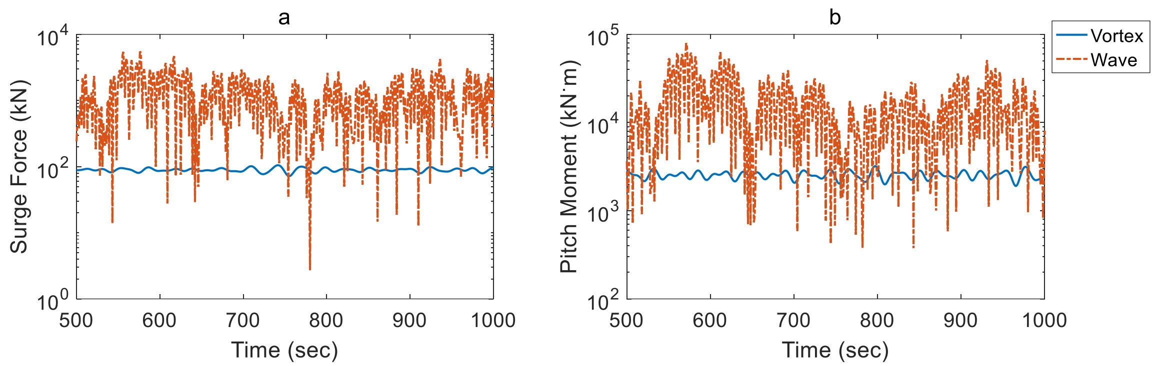

Fig.14 Magitude of drag and wave loads on the platform in LC3

4.4.3 Vertical Motions

Small difference is found in terms of the statistical results and time histories of heave in these three scenarios. Similar to the longitudinal motions, the response spectra in heave are almost identical in these cases. According to Fig. 15, although no additional load is applied on heave, the response slightly changed when the vortex excitation load is considered. This is due to the nonlinear coupling effect between heave and pitch modes. However, because the frequency of vortex shedding at the selected flow velocity is much higher than the natural frequency in heave, the current does not cause significant change in the response spectrum in heave.

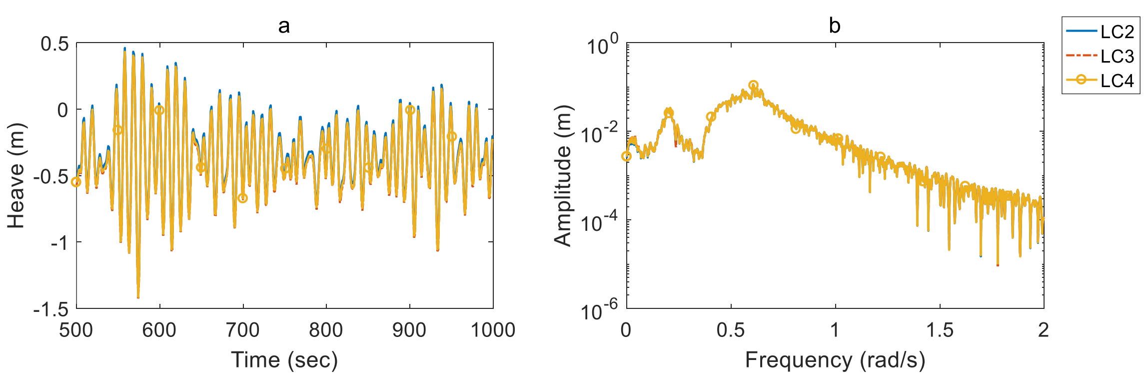

Fig.15 Time histories and response spectrum of heave

4.4.4 Tensions

According to the statistic results in Fig.8 and the time histories in Fig.16a, the effect of vortex shedding on mooring tension is similar to that on the longitudinal motions. That is to say, the mean tensions are significantly increased by the current due to the increasing surge displacement. On the other hand, we found that the oscillations are similar among 3 scenarios, based on the response spectra in Fig. 16b. The most significant responses are in the wave frequency, and the natural frequency (in surge). Therefore, the mooring tension is determined by the surge motion and incident wave, while the current has little effect on it.

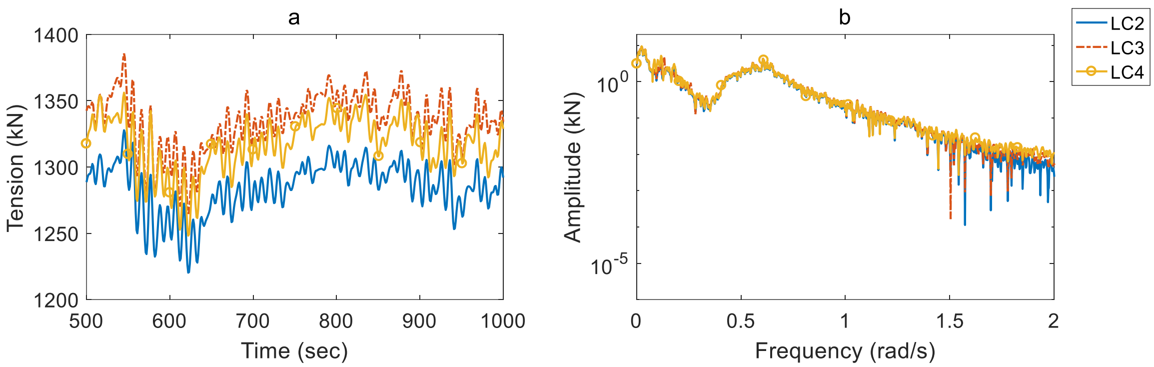

Fig.16 Time histories and response spectrum of tension in Line #2

5. Resonance and nonlinear coupling effect

According to the free-decay test, there exists nonlinear coupling effect among heave, roll and pitch. This effect, however, was not seen in the scenarios of rated sea states. This is attributed to the fact that the wave frequency is far from the natural frequencies in these DOF so that no resonance is excited. To further study the dynamic resonance and nonlinear response of the FOWT, two additional load cases (hereafter referred to as cases RU and RS) in which vortex shedding frequency is close to the natural frequency of roll, is examined. Based on the results of free-decay tests in Table.7 and vortex shedding frequencies in Fig.6b, the current velocity is chosen as 0.75m/s, corresponding to a vortex shedding frequency of 0.163 rad/s (same as the natural frequency in roll). In case RU, for simplicity, the frequency is applied to both parts of the buoy, and the flow is assumed to be uniform. On the other hand, a shear profile is used in case RS, which means that a portion of the profile has the current velocity corresponding to the shedding frequency close to the natural frequency in roll. Case 3 is chosen for comparison.

The motions in heave and roll are presented in Fig.17. Large amplitude of roll occurs in case R at the vortex shedding frequency (same as natural frequency in roll). Besides, a new peak at 0.3243 rad/s appears in the response spectrum of heave (Fig.17b). It is twice the vortex shedding frequency. This super-harmonic response is caused by the nonlinearly coupled restoring forces in heave and roll. Compared with the uniform flow case (Case RU), the resonant shear flow (Case RS) induces multi-frequency responses in roll, but the amplitude is much less than that of Case RU. On the other hand, the super-harmonic effect is not pronounced in the heave response of Case RS. This is due to the small amplitude of resonant response in roll.

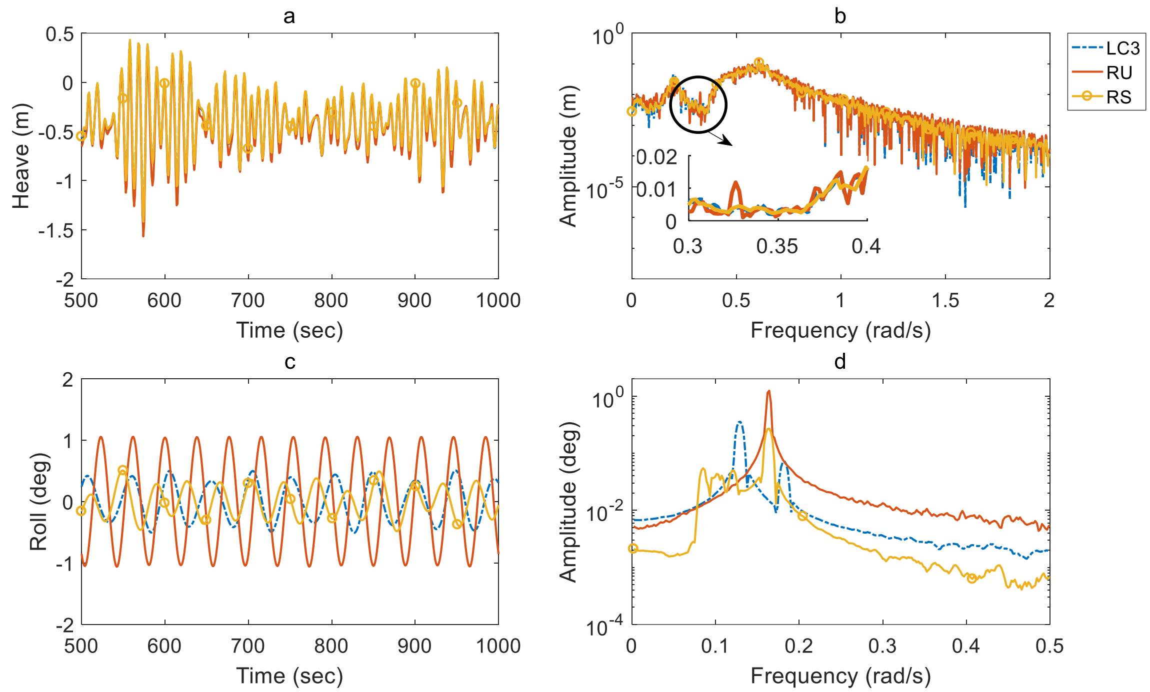

Fig.17 Resonance in roll and nonlinear coupling effect in heave

Therefore, when the wave, wind and current are all considered, the motion of SPAR-type FOWT may be affected significantly by vortex induced loads, especially in cases with resonance. In these cases, the amplified motion becomes a source of parametric excitation to affect responses in other DOF. For example, as illustrated above, due to the nonlinear coupling between heave and roll, resonance in roll induces super-harmonic (twice the vortex shedding frequency) response in heave. If this super-harmonic frequency happens to be close to the natural frequency in heave, it will in turn generate large response in heave. This is the internal resonance scenario found in SPAR-type offshore platforms [33].

6. Conclusions

A coupled dynamic model has been developed in time domain to investigate the dynamic responses of SPAR-type FOWT under the combined sea state of wind, wave and current. It includes a blade-element-momentum model of rotating blades, a nonlinear coupling hydrostatics model of floating structure, a three-dimensional nonlinear model of the free-surface effects on the SPAR buoy, a mooring model based on catenary theory, and a vortex-shedding model using computational fluid dynamics.

Based on this model, the motion of FOWT under the combined effects of vortex shedding, wave excitation, aerodynamic load and mooring load is calculated in time domain. The influence of both uniform current and shear current is analyzed. After the current is included, the vortex shedding will induce both lift loads and drag loads. The lift force and moment act directly on the sway and roll, causing transverse motions with the vortex shedding frequency. The drag force and moment are applied on the motions in the longitudinal direction. The mean position of surge is increased by the drag force. The oscillation in surge and the pitch motion are not significantly affected.

Compared with the uniform current, depth-dependent velocities of the shear current lead to variations of vortex shedding frequencies along the platform, which makes the frequencies of transverse motions more diversified. With the water depth increasing, the flow velocity decreases gradually, so do lift and drag. Therefore, the transverse motion caused by the shear current is smaller than that caused by the uniform flow with the same surface velocity. However, the flow profiles have no significant effect on longitudinal motion.

Due to the nonlinear coupling effect, the resonant lift load may affect not only roll but also other DOFs. For example, when the vortex shedding frequency is close to the natural frequency in roll, in addition to large resonance response in roll, large motion may also appear in heave at a super-harmonic frequency.

Although our simulations are conducted by using a specific design as an example, the results may have much broader implications. Firstly, these numerical studies suggest that the effects of current could be important for the response of FOWT. Therefore, such environmental condition should be taken into account during the design process. Moreover, both the lift and drag loads may cause responses in all DOFs. Neither of them should be neglected in the simulation. Finally, the coupling effect may create super-harmonic responses in heave mode, even leading to internal resonance at certain ratios of frequencies. These issues may cause potential dangers or damages.

It is necessary to point out that in the present work the interactions between wind and blades are modeled *via* the BEM theory. Though this classical algorithm has been widely used, the dynamic and unsteady effects are not included. To accurately simulate these effects, a dynamic model (e.g. three-dimensional potential theory [34,35]) may be adopted in the following study.

Besides, the vortex shedding is calculated *via* a 2D CFD model without considering the 3D effect. This may lead to inaccuracies in the prediction [36]. Future investigations about the 3D effect are required. Moreover, in this work we focus on resonance in roll, whereas the potential resonance in sway is not considered (as illustrated in our CFD simulation, in our particular case the vortex shedding frequency is much larger than the natural frequency in sway). However, in certain scenarios resonance in sway is observed [15]. Further study on this issue is also needed.

In reality, structural vibrations may affect the dynamic response as well as the environmental loads on the structure, especially for slender bodies such as mooring cables, blades and the tower. In the present study, the flexibility of these structures is not included. To analyze these issues more thoroughly, further simulations about the aero-elastic or hydro-elastic effects are needed.

Acknowledgments

The paper was financially supported by Nation Natural Science Foundation of China (Project No. 51479134), Research Fund of the State Key Laboratory of Ocean Engineering, Shanghai JiaoTong University (No.1501) and Natural Science Foundation of Tianjin (No.16JCYBJC21200). These sources of support are gratefully acknowledged. The support provided by China Scholarship Council (CSC No. 201606250066) during a visit of Yan Li to UCSD is acknowledged.

Reference

1. Weinzettel J, Reenaas M, Solli C, Hertwich EG. Life cycle assessment of a floating offshore wind turbine. Renewable Energy 2009; 34(3): 742-747.
2. Sun X, Huang D, Wu G. The current state of offshore wind energy technology development. Energy. 2012; 41(1): 298-312.
3. Chan G, Sclavounos PD, Jonkman J, Hayman G. Computation of Nonlinear Hydrodynamic Loads on Floating Wind Turbines Using Fluid-Impulse Theory. In: ASME 2015 34th International Conference on Ocean, Offshore and Arctic Engineering. St. John's, Newfoundland, Canada; May 2015.
4. Jeon M, Lee S, Lee S. Unsteady aerodynamics of offshore floating wind turbines in platform pitching motion using vortex lattice method. Renewable Energy 2014; 65: 207-212.
5. Hsu W, Thiagarajan KP, Manuel L. Extreme mooring tensions due to snap loads on a floating offshore wind turbine system. Marine Structures 2017; 55: 182-199.
6. Lopez-Pavon C, Watai RA, Ruggeri F, Simos AN, Souto-Iglesias A. Influence of Wave Induced Second-Order Forces in Semisubmersible FOWT Mooring Design. Journal of Offshore Mechanics and Arctic Engineering 2015; 137(3): 031602.
7. Robertson AN, Jonkman JM. Loads analysis of several offshore floating wind turbine concepts. In: The Twenty-first International Offshore and Polar Engineering Conference. International Society of Offshore and Polar Engineers. Maui, Hawaii, USA; June 2011.
8. Low YM, Srinil N. VIV fatigue reliability analysis of marine risers with uncertainties in the wake oscillator model. Engineering Structures 2016; 106: 96-108
9. Mukundan H, Modarres-Sadeghi Y, Dahl JM, Hover FS, Triantafyllou MS. Monitoring VIV fatigue damage on marine risers. Journal of Fluids and structures 2009; 25(4): 617-628.
10. Ulveseter JV, Svein S, Carl ML. Time domain model for calculation of pure in-line vortex-induced vibrations. Journal of Fluids and Structures 2017; 68: 158-173.
11. Ma P, Wei Q, Don S. Numerical Vortex-Induced Vibration Prediction of Marine Risers in Time-Domain Based on a Forcing Algorithm. Journal of Offshore Mechanics and Arctic Engineering 2014;136(3): 031703.
12. Ulveseter JV, Svein S, Carl ML. Vortex Induced Vibrations of Pipelines with Non-Linear Seabed Contact Properties. In ASME 2016 35th International Conference on Ocean, Offshore and Arctic Engineering. American Society of Mechanical Engineers. Busan, South Korea; June 2016.
13. Benitz MA, Schmidt DP, Lackner MA, Stewart GM, Jonkman J, Robertson A. Validation of

Hydrodynamic Load Models Using CFD for the OC4-DeepCwind Semisubmersible. In ASME 2015 34th International Conference on Ocean, Offshore and Arctic Engineering (pp. V009T09A037-V009T09A037). American Society of Mechanical Engineers. St. John's, Newfoundland, Canada; May 2015

14. Kokubun K, Ishida S, Nimura T, Chujo T, Yoshida S, Utsunomiya T. Model experiment of a SPAR type offshore wind turbine in storm condition. In ASME 2012 31st International Conference on Ocean, Offshore and Arctic Engineering (pp. 569-575). American Society of Mechanical Engineers. Rio de Janeiro, Brazil. July 2012.
15. Duan F, Hu Z, Wang J. Investigation of the VIMs of a SPAR-type FOWT using a model test method. Journal of Renewable and Sustainable Energy 2016; 8(6): 063301.
16. Wu C, Ma S, Kang C, Lim TBA, Jaiman RK, Weymouth G, Tutty O. Vortex-Induced Motion of a Square Cylinder at Moderate Reynolds Numbers. In ASME 2016 35th International Conference on Ocean, Offshore and Arctic Engineering, pp. V002T08A068-V002T08A068. American Society of Mechanical Engineers, Busan, South Korea; June 2016.
17. Hirabayashi S. Numerical analysis of vortex-induced motion of two-dimensional circular cylinder by lattice Boltzmann method. Journal of Marine Science and Technology 2016; 21(3): 426-433.
18. Minoru H, Hirabayashi S, Suzuki H. Experimental study of shape effect of floating body for Vortex-Induced Motion. In Techno-Ocean (Techno-Ocean), pp. 74-79. IEEE, 2016.
19. Liu M, Xiao L, Liang Y, Tao L. Experimental and numerical studies of the pontoon effect on vortex-induced motions of deep-draft semi-submersibles. Journal of Fluids and Structures 2017; 72: 59-79.
20. Liang Y, Tao L, Xiao L, Liu M. Experimental and numerical study on vortex-induced motions of a deep-draft semi-submersible. Applied Ocean Research 2017; (67): 169-187.
21. Liu SX. Study on the Nonlinear Coupled Motion of a SPAR under Stochastic Wave and Vortex, M. Eng. Degree Dissertation, Tianjin University, 2016
22. Jonkman J, Butterfield S, Musial W, Scott G. Definition of a 5-MW reference wind turbine for offshore system development. National Renewable Energy Laboratory, Golden, CO, Technical Report No. NREL/TP-500-38060. 2009
23. Jonkman, JM. Definition of the Floating System for Phase IV of OC3. National Renewable Energy Laboratory. 2010
24. Journée JMJ, Massie WW. Offshore hydromechanics. TU Delft, 2000.
25. Li J, Tang Y, Yeung RW. Effects of second-order difference-frequency wave forces on a new floating platform for an offshore wind turbine. Journal of Renewable and Sustainable Energy 2014; 6(3): 033102.
26. Li J, Jiang Y, Tang Y, Qu X, Zhai J. Effects of Second-Order Difference-Frequency Wave Forces on Floating Wind Turbine Under Survival Condition. Transactions of Tianjin University 2017; 23(2): 130-137.
27. Min H, Peng C, Duan F, Hu Z, Zhang J. Numerical Simulation of Dynamics of a SPAR Type Floating Wind Turbine and Comparison with Laboratory Measurements. In ASME 2016 35th International Conference on Ocean, Offshore and Arctic Engineering. American Society of Mechanical Engineers. Busan, South Korea; June 2016.
28. Melis C, Caille F, Perdrizet T, Poirette Y, Bozonnet P. A Novel Tension-Leg Application for Floating Offshore Wind: Targeting Lower Nacelle Motions. In ASME 2016 35th International Conference on Ocean,

Offshore and Arctic Engineering. American Society of Mechanical Engineers. Busan, South Korea; June 2016.

29. Moriarty PJ, Hansen AC. AeroDyn theory manual (No. NREL/TP-500-36881). National Renewable Energy Lab., Golden, CO (US). 2005
30. Tang Y, Li Y, Liu L, Jin W, Qu X. Study on Influence of Vortex Induced Loads on the Motion of SPAR-Type Wind Turbine Based on Aero-Hydro-Vortex-Mooring Coupled Model. In: ASME 2017 36th International Conference on Ocean, Offshore and Arctic Engineering; Trondheim, Norway; June, 2017
31. Li W, Tang YG, Liu LQ, Li Y, Wang B. Internal resonances for heave, roll and pitch modes of a SPAR platform considering wave and vortex-induced loads in the main roll resonance. China Ocean Engineering 2017; 31(4): 408-417.
32. Li W, Tang Y, Liu L, Liu S, Cai R. Heave-roll-pitch coupled nonlinear internal resonance response of a SPAR platform considering wave and vortex exciting loads. Journal of Ocean University of China 2017; 16(2): 209-222
33. Zhao J, Tang Y, Shen W. A study on the combination resonance response of a classic spar platform. Journal of vibration and control 2010; 16(14): 2083-2107.
34. Salehyar S, Li Y, Zhu Q. Fully-coupled time-domain simulations of the response of a floating wind turbine to non-periodic disturbances. Renewable Energy 2017; 111: 214-226.
35. Salehyar S, Zhu Q. Aerodynamic dissipation effects on the rotating blades of floating wind turbines. Renewable Energy 2015; 78: 119-127.
36. Gu JY, Zhu XY, Yang JM, Lu YX, Xiao LF. Numerical study on the 3-D complex characteristics of flow around the hull structure of TLP. China Ocean Engineering 2015; 29(4): 535-550.
37. Faltinsen, OM. Sea loads on ships and offshore structures. New York, NY (United States); Cambridge University Press, 10(1), 1993.
38. Wang Y, Yang J, Li X. CFD Analysis of unsteady flows around a new cell-truss spar and the corresponding vortex-induced motions. In :ASME 2008 27th International Conference on Offshore Mechanics and Arctic Engineering. American Society of Mechanical Engineers, 2008.
39. Li Z, Yao W, Yang K, Jaiman RK, and Khoo BC. On the vortex-induced oscillations of a freely vibrating cylinder in the vicinity of a stationary plane wall. Journal of Fluids and Structures, 2016; 65: 495-526.
40. Navrose, Mittal S. Free vibrations of a cylinder: 3-D computations at Re= 1000[J]. Journal of Fluids and Structures, 2013, 41: 109-118.
41. Bourguet R, Karniadakis GE, Triantafyllou MS. Multi-frequency vortex-induced vibrations of a long tensioned beam in linear and exponential shear flows. Journal of Fluids and Structures, 2013; 41: 33-42.
42. Wang E, Xiao Q, Incecik A. CFD simulation of vortex-induced vibration of a vertical riser. In: Proceedings of the 9th International Workshop on Ship and Marine Hydrodynamics, 26 – 28 August 2015, Glasgow, UK
43. Wang E, Xiao Q, Incecik A. Three-dimensional numerical simulation of two-degree-of-freedom VIV of a circular cylinder with varying natural frequency ratios at Re= 500. Journal of Fluids and Structures, 2017; 73: 162-182.
44. Wang, E., Xiao, Q., Zhu, Q. & Incecik, A. (2017) " The effect of spacing on the vortex-induced vibrations of two tandem flexible cylinders." Physics of Fluids. 29(7): 077103.

45. Vandiver JK. Research challenges in the vortex-induced vibration prediction of marine risers. In: Proceedings of Offshore Technology Conference. Offshore Technology Conference, 1998.
46. Wang Y. Research on the key characteristics of SPAR vortex-induced motions. Ph. D. Dissertation, Shanghai Jiao Tong University, 2010
47. Fan JJ. Numerical Simulation of Fluid-Structural Interaction for Vortex-Induced Vibration of deep-sea top tension risers. M Eng. Degree Dissertation, Tianjin University, 2016
48. Hover FS, Techet AH, Triantafyllou MS. Forces on oscillating uniform and tapered cylinders in cross flow. Journal of Fluid Mechanics. 1998; 363: 97-114.
49. Lucor D, Triantafyllou MS. Parametric study of a two degree-of-freedom cylinder subject to vortex-induced vibrations. Journal of Fluids and Structures. 2008; 24(8): 1284-1293.
50. Zhao M, Cheng L, An H, and Lu L Three-dimensional numerical simulation of vortex-induced vibration of an elastically mounted rigid circular cylinder in steady current. Journal of Fluids & Structures, 2014; 50:292-311.

Figure Captions List